2023

A Ten-Fold Solvent Kinetic Isotope Effect for the Nonradiative Relaxation of the Aqueous Ferrate(VI) Ion

Cali Antolini
University of Rhode Island

Danielle J. Jacoby
University of Rhode Island

Sophia M. Tiano
University of Rhode Island

Christopher J. Otolski

Gilles Doumy

See next page for additional authors

Citation/Publisher Attribution

Antolini, Cali, Danielle J. Jacoby, Sophia M. Tiano, Christopher J. Otolski, Gilles Doumy, Anne M. March, Donald A. Walko, Joseph E. Goodwill, and Dugan Hayes. "A Ten-Fold Solvent Kinetic Isotope Effect for the Nonradiative Relaxation of the Aqueous Ferrate(VI) Ion." *The Journal of Physical Chemistry A* 127, 49 (2023). doi: 10.1021/acs.jpca.3c06042.

A Ten-Fold Solvent Kinetic Isotope Effect for the Nonradiative Relaxation of the Aqueous Ferrate(VI) Ion

Authors

Cali Antolini, Danielle J. Jacoby, Sophia M. Tiano, Christopher J. Otolski, Gilles Doumy, Anne Marie March, Donald A. Walko, Joseph E. Goodwill, and Dugan Hayes

A Ten-Fold Solvent Kinetic Isotope Effect for the Nonradiative Relaxation of the Aqueous Ferrate(VI) Ion

Cali Antolini,[†1] Danielle J. Jacoby,[1] Sophia M. Tiano,[1] Christopher J. Otolski,[2] Gilles Doumy,[2] Anne Marie March,[2] Donald A. Walko,[3] Joseph E. Goodwill,[4] and Dugan Hayes[1]*

[1]Department of Chemistry, University of Rhode Island, Kingston, Rhode Island 02881, USA

[2]Chemical Sciences and Engineering Division, Argonne National Laboratory, Argonne, Illinois 60439, USA

[3]Advanced Photon Source, Argonne National Laboratory, Argonne, Illinois 60439, USA

[4]Department of Civil and Environmental Engineering, University of Rhode Island, Kingston, Rhode Island 02881, USA

KEYWORDS. ferrate, transient absorption spectroscopy, solvent kinetic isotope effect

ABSTRACT. Hypervalent iron intermediates have been invoked in the catalytic cycles of many metalloproteins, and thus it is crucial to understand how the coupling between such species and their environment can impact their chemical and physical properties in such contexts. In this

work, we take advantage of the solvent kinetic isotope effect (SKIE) to gain insight into the nonradiative deactivation of electronic excited states of the aqueous ferrate(VI) ion. We observe an exceptionally large SKIE of 9.7 for the nanosecond-scale relaxation of the lowest energy triplet ligand field state to the ground state. Proton inventory studies demonstrate that a single solvent O-H bond is coupled to the ion during deactivation, likely due to the sparse vibrational structure of ferrate(VI). Such a mechanism is consistent with that reported for the deactivation of *f-f* excited states of aqueous trivalent lanthanides, which exhibit comparably large SKIE values. This phenomenon is ascribed entirely to dissipation of energy into a higher overtone of a solvent acceptor mode, as any impact on the apparent relaxation rate due to a change in solvent viscosity is negligible.

INTRODUCTION

The ferrate(VI) ion, $[FeO_4]^{2-}$, is a uniquely stable Fe(VI) complex that can serve as a convenient model for hypervalent iron complexes that are air-sensitive, short-lived, or otherwise challenging to characterize. Such species play key roles in the catalytic cycles of hemoproteins such as cytochrome P450[1–3] as well as a broad variety of non-heme oxygenases[4–6] that carry out halogenation,[7] hydroxylation,[8] epoxidation,[9] and olefination[10] reactions.

The optical absorption spectrum of ferrate(VI) (Fig. S1A) was extensively studied throughout the latter half of the 20th century.[11–16] We recently reviewed that foundational work and reported the first time-resolved measurements of the excited state dynamics of the ion using a combination of optical and X-ray spectroscopies.[17] Briefly, the ultraviolet (UV) absorption bands

of ferrate(VI) are comprised of ligand-to-metal charge transfer (LMCT) transitions, while the visible absorption band centered at 560 nm corresponds to two clusters of $^3A_2 \rightarrow {}^3T_1$ ligand field (or metal-centered, MC) transitions.[16] Following UV excitation into the ^{3}LMCT states, branching between the intersystem crossing (ISC) and internal conversion (IC) pathways occurs on the timescale of tens of ps, with only ~15% of the population undergoing ISC to reach the ^{5}LMCT state from which the highly oxidizing metastable $[FeO_3OH]^{2-}$ species forms; the remainder relaxes to the ground state through the manifold of ^{3}MC states.[17] Crucially for the work presented here, we also found that ground state recovery occurs nonradiatively from the $^3T_2$ MC state with a time constant of 3.8 ns.

Nevertheless, many questions regarding the photophysical and photochemical dynamics of aqueous ferrate(VI) remain. For example, we proposed that the IC time constants (8 ps and 3.8 ns for the ^{3}LMCT $\rightarrow {}^3T_1$ and $^3T_2 \rightarrow {}^3A_2$ processes, respectively) are unusually long because the excited state geometries are not substantially distorted from that of the ground state, resulting in a nested arrangement of the potential energy surfaces, but this hypothesis needs to be evaluated experimentally. Similarly, our tentative assignment of the observed 250 ps time constant to hydrogen atom abstraction from the solvent by the ^{5}LMCT state to form $[FeO_3OH]^{2-}$ was not supported by direct evidence. We thus sought to explore these questions further by measuring the solvent kinetic isotope effect(s) (SKIEs) for these photoinduced processes.

While the more familiar kinetic isotope effect (KIE) quantifies a change in reaction rate upon isotopic substitution of a reactant, the SKIE quantifies a change in rate of *any* process upon isotopic substitution of the solvent in which the process occurs. It is important to note that, perhaps confusingly, the term SKIE rather than KIE applies to reactions in which the solvent also participates as a reactant – in the rate determining step, or even simply in the overall reaction

scheme. Common examples include proton transfer,[18–20] hydrogen abstraction,[21–23] and hydrolysis reactions,[24] and such studies have been particularly informative for elucidating the catalytic cycles of enzymes[25–27] and the mechanisms of water oxidation in both natural[28,29] and artificial[30–33] systems. Proton inventory studies, wherein the relative concentrations of protonated and deuterated solvent is varied, may also be used to determine the number of protons involved in the rate determining step for reactions in protic solvents.[34–39]

Because the SKIE is relevant whenever solvent vibrations are involved in mediating a process, such studies may also be used to investigate photophysical phenomena in solution. As discussed by Robinson and Frosch, the dependence of radiationless transition rates on isotopic substitution is determined by both the electronic energy gap and the availability of high frequency vibrational modes through which the energy may be dissipated.[40–42] Accordingly, SKIE values close to unity are common for IC and ISC processes connecting excited states close in energy, and only modest increases are typically observed in the luminescence lifetimes of many organic dyes.[43–45] Solvated lanthanide ions, on the other hand, only possess vibrational modes in the context of their solvation shell, and consequently, large SKIE values in excess of 10 have been reported for the deactivation of their *f-f* excited states.[46–52]

Such a large increase in nonradiative lifetime is generally attributed to the increase in the number of vibrational quanta needed to span the electronic energy gap by the lower frequency O-D (vs. O-H) stretch and the attendant lower probability of exciting the higher overtone of the acceptor mode.[47] For example, aqueous Dy^{3+} and Eu^{3+} ions – which have the closest *f-f* energy gaps among the trivalent lanthanides to that of the $^3A_2 \rightarrow {}^3T_2$ transition in ferrate(VI) – require approximately three and four O-H vibrational quanta to dissipate their respective 7,850 and 12,300 cm^{-1} of electronic energy. This increases to four and five quanta for the O-D vibration,

and consequently the nonradiative decay rate constants decrease by factors of 180 and 18, respectively, in D_2O.[49–51,53] For macrocyclic Eu^{3+} complexes, however, where energy may be exchanged with the ligand, single-digit SKIE values may be observed.[54]

In 1966, Heller showed that nonradiative relaxation of aqueous lanthanide ions occurs through coupling to a single O-H bond and thus through an overtone of that vibration.[55] Eqns. 1 and 2 have since been used to calculate q, the number of O-H bonds that are within the inner coordination sphere of a lanthanide complex:[50,53,56]

$$k^{H_2O} = k_{rad} + k_{nr} + qk_{H_2O}, \qquad k^{D_2O} = k_{rad} + k_{nr} + qk_{D_2O} \tag{1}$$

$$\Delta k = k^{H_2O} - k^{D_2O} = q\left(k_{H_2O} - k_{D_2O}\right) \tag{2}$$

Here, k^{H_2O} and k^{D_2O} are the luminescent rate constants measured in those solvents, k_{rad} is the radiative decay rate constant, k_{nr} is the nonradiative decay rate constant from all processes not involving water, and k_{H_2O} and k_{D_2O} are the nonradiative decay rate constants due to a single H_2O or D_2O molecule, respectively. Subtracting the measured rate constants eliminates all contributions to the luminescence decay that do not involve water, leaving the simple expression given in Eqn. 2. It is important to note, however, that it is only possible to know the values of q, k_{H_2O}, and k_{D_2O} if two of the three may be independently measured. Using X-ray crystallography to measure q for a series of Eu^{3+} and Tb^{3+} complexes, Horrocks and Sudnick showed that Δk is indeed directly proportional to q;[53,56] thus, q may be estimated from the value of Δk measured for any complex of a metal for which the slope $k_{H_2O} - k_{D_2O}$ has been similarly determined.

In this work, we report the SKIE for the nonradiative ground state recovery of the aqueous ferrate(VI) ion, which occurs from the $^3T_2$ state. We have measured the nonradiative decay rates in H_2O and D_2O buffer solutions using both optical transient absorption (OTA) and X-ray transient absorption (XTA) spectroscopies on the nanosecond timescale and have also performed

an OTA proton inventory study to determine the number of solvent acceptor modes that facilitate this transition. Importantly, we do not observe a significant viscosity dependence for the ground state recovery rate. These results are presented in the context of the nonradiative deactivation of lanthanide ions and small organic chromophores, and the bioinorganic implications of this work are briefly discussed.

EXPERIMENTAL METHODS

Sample preparation. Samples were prepared at room temperature by dissolving potassium ferrate(VI) (>92% purity, Element 26 Technology) in phosphate/borate buffer (5 mM disodium phosphate and 0.25 mM sodium tetraborate, Fisher Scientific) prepared using distilled water and/or deuterium oxide (Cambridge Isotope Laboratories). For viscosity measurements, the buffer solution also contained 5 M sodium chloride. The concentration of potassium ferrate(VI) was 2.5 mM for all XTA experiments (OD = 1.59 at 266 nm and 0.44 at 532 nm), 2.0 mM for all OTA experiments with UV excitation (OD = 1.23 at 267 nm), and 4.0 mM for OTA experiments with visible excitation to account for the lower absorptivity of the ligand field band (OD = 0.59 at 560 nm). Samples were then filtered to remove insoluble material using either 1.0 μm syringe filters or Grade 1 filter paper and measured within one hour of preparation.

Optical transient absorption. All OTA measurements were conducted as previously described[17] with two modifications described below. Briefly, the third harmonic (267 nm) of the output of a commercial regeneratively amplified Ti:sapphire laser (Astrella, Coherent, Inc.) was used as the pump beam for femtosecond-resolved measurements, focused at the sample position to a spot size ($1/e^2$ diameter) of 300 μm (0.35 mJ/cm^2 fluence). The output of a commercial diode pumped Q-switched Nd:YAG laser and OPO (NT242, EKSPLA) was used as the pump for

nanosecond measurements. For nanosecond measurements with 267 nm excitation, the pump energy was 3.4 μJ/pulse at the sample position with an anisotropic spot size of 1.5 x 0.4 mm (0.57 mJ/cm^2 fluence). For nanosecond measurements with 560 nm excitation, the pump energy in the same spot size was 18 μJ/pulse (3.0 mJ/cm^2 fluence). The sample was delivered to the pump-probe overlap position through a 0.5 mm pathlength quartz flow cell cuvette using a peristaltic pump. Data acquisition for all OTA experiments was accomplished using virtual instruments written in-house (LabVIEW 2017, National Instruments).

For our previous femtosecond-resolved experiments, we had used a sapphire plate to generate the white light probe spectrum.[17] For the same experiments reported here, however, the white light probe was generated by focusing a portion of the fundamental beam into the center of a 5 cm pathlength quartz cuvette filled with distilled water and passing the resulting white light through a short-pass filter (750 nm cut-off), which furnished a continuous spectrum that spanned from 385 to 750 nm. This is much broader than the spectrum we previously achieved using sapphire, which did not extend to wavelengths shorter than 450 nm. The other modification made here was that the sample cuvette was continuously raster scanned at a rate of ~1 mm/min to prevent accumulation of insoluble decomposition products at the pump beam position.

X-ray transient absorption. High repetition rate XTA experiments were performed at beamline 7-ID-D at the Advanced Photon Source (APS, Argonne National Laboratory) as previously described.[17,57–59] Briefly, iron K-edge transient absorption spectra were acquired in total fluorescence yield at repetition rates of 1.30 MHz for the optical pump and 6.52 MHz for the X-ray probe (24-bunch mode of the APS), with the laser oscillator phase-locked to the RF reference signal from the storage ring. The second (532 nm) or fourth (266 nm) harmonic of an oscillator power amplifier Nd:YVO_4 laser system (Duetto, Time-Bandwidth/Lumentum) was used as the

optical pump, with a spot size of 51 μm (1/e^2 diameter) at the sample. For measurements with 532 nm excitation, the pump energy was 0.42 μJ/pulse (20 mJ/cm^2 fluence), while for measurements with 266 nm excitation, the pump energy was 0.33 μJ/pulse (16 mJ/cm^2 fluence). The Gaussian instrument response function (IRF) was measured to be 94 ps (FWHM). The X-ray spot size at the sample position was 8.5 x 8.5 μm (1/e^2 full width). The sample was delivered to the pump-probe overlap position as a 130 μm diameter free-flowing liquid jet using a high-performance liquid chromatography pump.

Data analysis. All data analysis was performed using MATLAB R2019a (MathWorks). Kinetic traces were fit using the nonlinear regression function nlinfit. All kinetic traces were fit to the sum of one or more exponential decay components and in some cases a step function, all convolved with a common Gaussian IRF and a variable time zero; detailed descriptions of this procedure and our decay-associated analysis methods are given in our previous report.[17] The width of the IRF was included as a variable parameter in all fits, and the resulting values were: 75 ± 5 fs for femtosecond-resolved OTA; 0.6 ± 0.3 ns for nanosecond-resolved OTA; and 75 ± 8 ps for XTA. Time constants are reported with 95% confidence intervals, which were obtained by multiplying the square roots of the diagonal elements of the corresponding covariance matrices by a factor of 1.96.

The temporal chirp of the white light probe pulse used in the femtosecond-resolved OTA experiments was corrected by fitting the time delay corresponding to the maximum of the coherent artifact at each wavelength to the sum of a second-order polynomial and a logarithmic term. The time grid at each wavelength was then shifting by the corresponding value of this function and interpolated back onto the original time grid using a cubic spline to align all delay times across the bandwidth of the probe spectrum. We note that only the femtosecond-resolved

OTA *spectra* presented here were taken from the chirp-corrected data; because the temporal chirp is negligible within narrow ranges of the probe bandwidth (<10 nm), the kinetic traces were taken from the raw data.

RESULTS AND DISCUSSION

Ultrafast optical transient absorption. In our previous work,[17] we measured a 250 ps decay in the excited state absorption (ESA) of aqueous potassium ferrate(VI) at pH 8.6 following UV excitation at 267 nm and tentatively assigned this time constant to conversion of the ^{5}LMCT state to $[FeO_3OH]^{2-}$, the metastable but dominant ferrate(V) species at this pH identified by Bielski, Rush, Sharma, and coworkers through pulse radiolysis.[60–65] We hypothesized that this process could occur either in a single step (hydrogen atom transfer) or through sequential proton and electron transfer steps. To confirm this assignment, we repeated our femtosecond-resolved OTA measurements of ferrate(VI) following UV excitation in a buffer solution prepared with D_2O instead of H_2O. The OTA spectra in H_2O and D_2O buffers are shown in Figs. 1A and 1B, respectively. The shapes of the spectra in the two buffers are essentially indistinguishable but differ somewhat in shape from those presented in our previous report[17] due to the broader bandwidth and improved focal properties of the white light probe beam in the current realization of our instrument. Most notably we resolve an additional feature centered at 535 nm that decays with a time constant of 46 ± 4 ps in H_2O and 58 ± 5 ps in D_2O (Fig. S2), in excellent agreement with the 45 ps time constant we previously assigned to ISC. By 2 ns, the spectra very closely resemble the earliest spectra measured in our nanosecond-resolved experiments (*vide infra*), but the concave region between 400 and 600 nm is notably flatter in the H_2O buffer; this is discussed later.

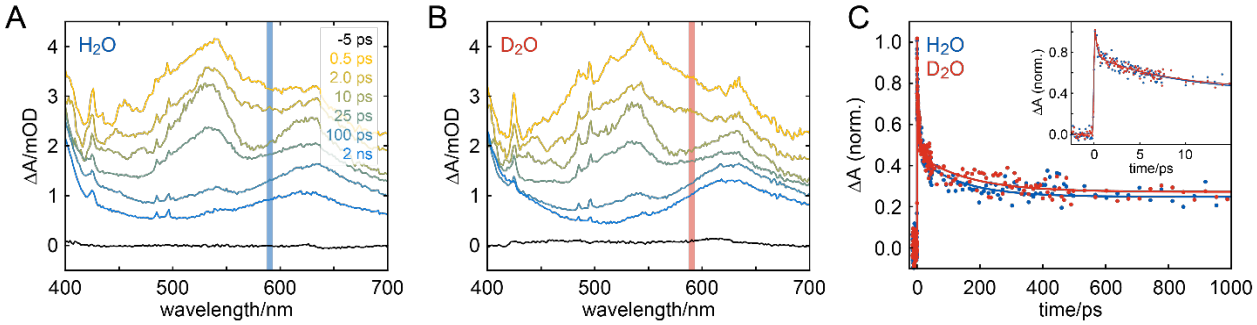

Figure 1. Ultrafast OTA spectra and kinetics of potassium ferrate(VI) following excitation at 267 nm. (A) Spectra in H_2O buffer solution at various delay times, showing a broad ESA that spans the probe bandwidth. (B) Spectra in D_2O buffer solution. (C) Kinetic traces (dots) in H_2O (blue) and D_2O (red) obtained by averaging the OTA signals over the probe region centered at 590 nm indicated by the vertical bars in panels (A) and (B) that have then been normalized to the maxima of the corresponding multi-exponential fits (solid curves). The two traces show strong qualitative agreement on the sub-ns timescale. (Inset) Early delay times of the same traces and fits.

We have previously shown that analysis of the ultrafast dynamics of aqueous ferrate(VI) following excitation into the LMCT state may be substantially simplified by first considering the kinetic trace taken at a probe wavelength of 590 nm, where relaxation between MC states does not contribute to the decay of the signal.[17] The kinetic traces averaged over the probe bandwidth spanning 587 to 593 nm in both buffers are plotted in Fig. 1C with their corresponding fits to the sum of three exponential decay components and a step function ($\tau_4 > 3$ ns), all convolved with a Gaussian IRF; the fits are also plotted with their individual components in Fig. S3. The time constants are given with their respective 95% confidence intervals in Table 1, and a simplified

Jablonski diagram summarizing the assignments of the time constants reported here is given in Fig. S4. As expected, the first two time constants (corresponding to thermalization and IC, respectively) are in excellent agreement between the two buffers, showing that any SKIE is negligible for these ultrafast processes. And while the third time constant appears to be marginally longer in D_2O vs. H_2O, the difference is less than half the magnitude of the corresponding confidence intervals. Increasing the averaging time for both samples to improve the signal to noise ratio could allow us to perform a quantitative comparison, but the short lifetime of each sample (< 1 h) compounded by both our limited access to high-purity potassium ferrate(VI) and the high cost of D_2O makes such efforts impractical. Instead, we simply conclude here that if an SKIE does exist for the ~140 ps decay component, it is too small to measure with the current data and is likely well below 2.0. We also note that the third time constant in H_2O is a refinement of that given in our previous report[17] with a substantially narrower confidence interval.

Table 1. Ultrafast time constants measured at 590 nm following excitation at 267 nm

	H_2O	D_2O
τ_1 (ps)	0.19 ± 0.14	0.26 ± 0.15
τ_2 (ps)	8.1 ± 2.1	8.0 ± 2.0
τ_3 (ps)	140. ± 51	162 ± 53
τ_4 (ns)	> 3	> 3

Nanosecond transient absorption. Although the ultrafast dynamics appear largely unperturbed by the substitution of deuterated solvent, a dramatic change in the kinetics on the few- to tens-of-ns timescale is immediately evident. OTA and Fe K-edge XTA spectra and kinetics following excitation at 267 nm are plotted in Figs. 2A-D for ferrate(VI) in H_2O buffer and in Figs. 2E-H for ferrate(VI) in D_2O buffer; the ground state Fe K-edge spectrum in H_2O buffer is shown in Fig. S1B. At early delay times, the spectra in H_2O exhibit a strong ESA peak centered at 650 nm with a shoulder at 775 nm and a dip toward the baseline at 520 nm, but only a broad ESA spanning the entire probe bandwidth is apparent after 10 ns (Fig. 2A). We previously showed that the features of the early spectra reflect a mixture of the short-lived Fe(VI) $^3T_2$ state and the metastable Fe(V) LMCT states, while the featureless late spectra only reflect the LMCT states.[17] The evolution between the two extremes reflects the few-ns ground state recovery from the $^3T_2$ state, and because the IRF of our nanosecond OTA instrument is ~2 ns, a substantial amount of the $^3T_2$ state relaxes within the laser pulse envelope. In D_2O, however, the dip at 520 nm is clearly shown to be the ground state bleach (GSB) of the ligand field band, and the characteristic features of the $^3T_2$ state can be seen beyond 75 ns (Fig. 2E), suggesting that the ^{3}MC state persists much longer in the deuterated buffer.

As expected from these OTA results, the XTA spectra measured at 100 ps and 153 ns in H_2O (Fig. 2B) and D_2O (Fig. 2F) are essentially indistinguishable, as these delay times bookend the timeframe for decay of the $^3T_2$ state in either buffer. Both difference spectra at 100 ps show a positive peak at 7.1145 keV and a negative peak at 7.1160 keV that respectively correspond to partial depopulation of the *e* orbitals and population of the t_2 orbitals of the Fe 3*d* set within the tetrahedral ligand field upon formation of the $^3T_2$ state. By 153 ns, these features are gone, and both spectra only show a small dip at 7.1154 keV and a broad positive band along the rising edge

centered at 7.1273 keV, both of which correspond to the reduction of Fe(VI) to Fe(V) in the LMCT states.[17]

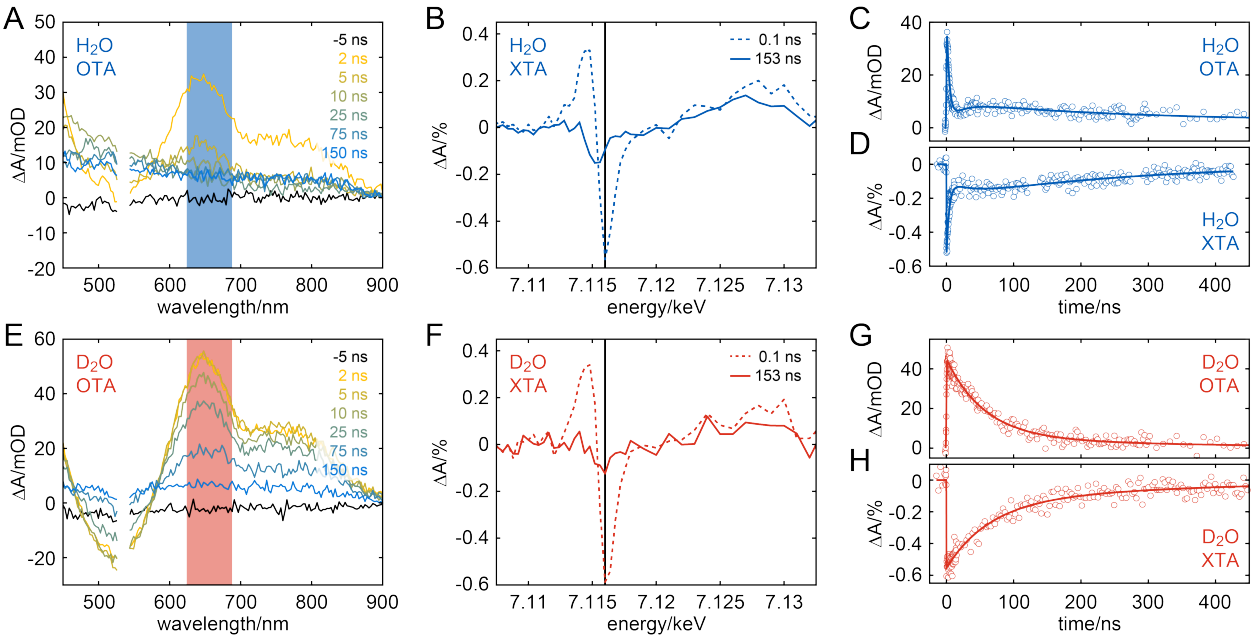

Figure 2. Nanosecond transient absorption spectra and kinetics of potassium ferrate(VI) following UV excitation at 267 nm. (A) OTA spectra in H_2O buffer at various delay times. (B) XTA spectra in H_2O buffer at 100 ps (dashed curve) and 153 ns (solid curve). (C) OTA kinetic trace (circles) and fit (solid curve) averaged over the probe bandwidth indicted by the blue vertical bar in panel (A). (D) XTA kinetic trace (circles) and fit (solid curve) measured at the probe energy indicted by the black vertical line in panel (B). (E) - (H) The same spectra and kinetic traces measured in D_2O buffer.

OTA kinetic traces averaged over the probe bandwidth spanning 625 to 685 nm are plotted with corresponding fits in Figs. 2C and 2G, and XTA kinetic traces measured at 7.1160 keV are plotted with corresponding fits in Figs. 2D and 2H. The two techniques show excellent

agreement for each sample, but significant differences between the dynamics of ferrate(VI) in the two environments are clear. The TA signals in H_2O are dominated by a fast, few-ns decay (ground state recovery from the $^3T_2$ state) and then exhibit weakly nonmonotonic behavior for the next ~50 ns as the total signal trends toward the baseline; we previously speculated that these slower dynamics were related to intermolecular reactions of Fe(V) species. In D_2O, however, the initial decay is markedly slower and obscures any nonmonotonic behavior. As a result, only two decay components are needed to model the data.

The kinetic traces in H_2O were fit to the sum of three exponential decay components and a step function ($\tau_7 > 10\ \mu s$) as in our previous work, but the traces in D_2O were well represented with only two exponential decays and a step function. The time constants from these fits are collected in Table 2, and the fits are shown with their individual components in Figs. S5A and S5C. The dynamics on the timescale of hundreds of ns are influenced in the high repetition rate XTA measurements by the sample flow rate, but the τ_6 value measured in H_2O is in good agreement with those measured by OTA in either buffer. A stable fit of the XTA kinetic trace measured in D_2O could only be obtained by fixing τ_6 to the value measured by OTA, but with that constraint in place, the values of τ_4 obtained from both fits (~60 ns) are in excellent agreement.

To confirm that the 60 ns time constant in D_2O corresponds to ground state recovery from the manifold of ^{3}MC states, we performed decay-associated analysis across the entire probe bandwidth of the nanosecond OTA spectra in both buffers. The decay-associated spectra (DAS) shown in Figs. S5B and S5D clearly demonstrate that the 4 ns decay in H_2O and 60 ns decay in D_2O both correspond to the same species – namely, the $^3T_2$ state, with its strong GSB at 520 nm and ESA peaks at 650 and 775 nm – while the slower time constants correspond to the featureless Fe(V) species. Remarkably, these results indicate that the substitution of D_2O for H_2O

extends the lifetime of the $^3T_2$ state by more than an order of magnitude but has little to no impact on the dynamics of the longer-lived Fe(V) species. This also explains the small but noticeable difference between the shapes of the femtosecond-resolved OTA spectra in the two buffers at late delay times: by 2 ns, the ^{3}MC state has decayed by ~40% in H_2O but only ~4% in D_2O, so the concavity between 400 and 600 nm originating from overlap of the GSB of the ^{3}MC state and the broad ESA of the ^{5}LMCT state is less apparent in H_2O.

Table 2. Nanosecond time constants measured by OTA and XTA

pump	ultraviolet				visible[a]			
solvent	H_2O		D_2O		H_2O		D_2O	
probe	XTA	OTA	XTA	OTA	XTA	OTA	XTA	OTA
τ_4 (ns)	4.2 ± 0.9	4.0 ± 1.0	63 ± 13	56 ± 6	4.0 ± 0.3	3.8 ± 1.0	49 ± 5	55 ± 2
τ_5 (ns)	33 ± 34	19 ± 20	x	x	x	x	x	x
τ_6 (ns)	270 ± 80	270 ± 90	320[b]	320 ± 340	x	x	x	x
τ_7 (μs)	x	> 10	x	> 10	x	x	x	x

[a]532 nm for XTA, 560 nm for OTA

[b]Value fixed in fit

We then repeated these measurements using visible excitation to circumvent the LMCT states and populate the ^{3}MC states directly, thereby further simplifying analysis. The same spectra and kinetic traces are shown in Fig. 3 following excitation at 560 nm (OTA) or 532 nm (XTA). While different wavelengths were employed due to experimental limitations at the beamline, we have previously shown that the dynamics of ferrate(VI) after the first few ps are entirely independent of excitation wavelength across the band of ^{3}T ligand field states and may be

represented with only a single exponential decay.[17] Because the LMCT states no longer contribute, the OTA spectra in both buffers look identical and only vary in their kinetics. As expected, the OTA and XTA kinetic traces in H_2O both fit to a single decay with a time constant of ~4 ns, while those in D_2O both fit to a single decay with a time constant of ~55 ns, further confirming the assignments of these to decay of the $^3T_2$ state.

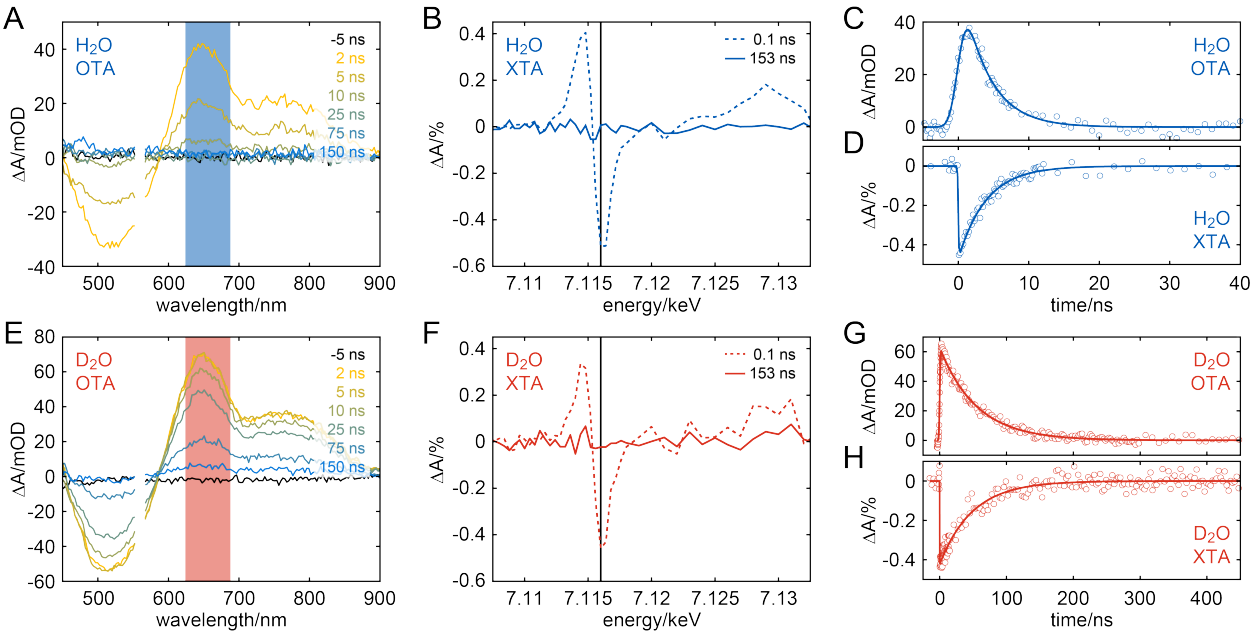

Figure 3. Nanosecond transient absorption spectra and kinetics of potassium ferrate(VI) following visible excitation at 560 nm (OTA) or 532 nm (XTA). (A) OTA spectra in H_2O buffer at various delay times. (B) XTA spectra in H_2O buffer at 100 ps (dashed curve) and 153 ns (solid curve). (C) OTA kinetic trace (circles) and fit (solid curve) averaged over the probe bandwidth indicted by the blue vertical bar in panel (A). (D) XTA kinetic trace (circles) and fit (solid curve) measured at the probe energy indicted by the black vertical line in panel (B). (E) - (H) The same spectra and kinetic traces measured in D_2O buffer. Note that the time axes of panels (C) and (D) are different from those of panels (G) and (H).

Solvent viscosity. Since H_2O and D_2O differ in viscosity (0.89 cP and 1.11 cP at 25°C, respectively),[66] we now evaluate the extent to which viscosity contributes to the striking increase in the $^3T_2$ lifetime in D_2O. Although the ferrate(VI) ion is too compact to exhibit the familiar viscosity-dependent relaxation dynamics arising from drag forces in "floppy" molecules like stilbene,[67] triarylmethanes,[68] and rhodamines,[69] intermolecular deactivation is a possibility. We have seen no variation in lifetime as a function of ferrate(VI) concentration, but such observations have been limited to the fairly narrow concentration range for which OTA measurements are possible (roughly 2 to 5 mM). Furthermore, the non-emissive nature of aqueous ferrate(VI) makes a conventional Stern-Volmer fluorescence measurement impossible. Accordingly, we repeated the OTA measurement in H_2O buffer supplemented with 5 M NaCl, which has a viscosity more than 70% higher than that of the standard H_2O buffer (1.53 cP at 25°C).[70] Although the dramatically higher ionic strength of this buffer could also impact the relaxation, all solvent systems prepared by adding viscous polyols (e.g., glycerol, (poly)ethylene glycol, polyvinyl alcohol) to the H_2O buffer caused ferrate(VI) to convert to insoluble Fe(III) oxides within minutes.

OTA spectra of ferrate(VI) in H_2O buffer containing 5 M NaCl following visible excitation at 560 nm are shown in Fig. 4A, and the kinetic trace and fit (olive dots and solid curve) are plotted in Fig. 4B alongside those measured in standard H_2O (blue) and D_2O (red) buffers. The fit of the 5 M NaCl data reveals a lifetime of 4.7 ± 0.3 ns, which is approximately 25% longer than that in standard H_2O buffer but still within the 95% confidence interval. Thus, while the $^3T_2$ lifetime may show some small viscosity dependence, we conclude that any increase in lifetime due to viscosity alone is negligible compared to the tenfold increase observed in D_2O.

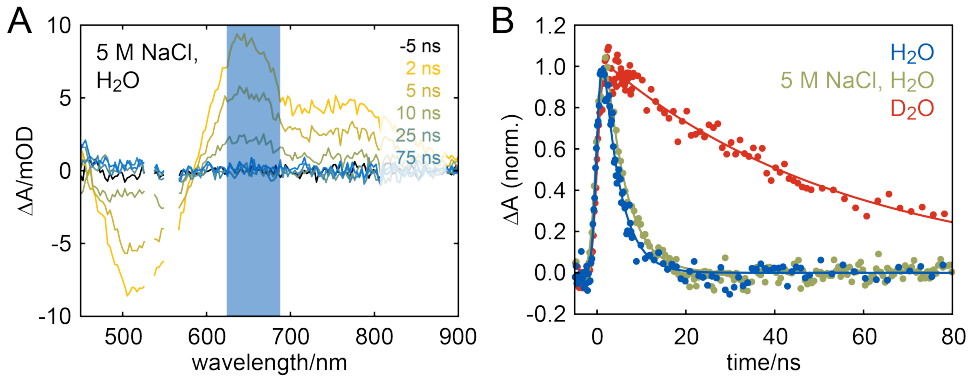

Figure 4. Viscosity dependence of potassium ferrate(VI) relaxation dynamics following visible excitation at 560 nm. (A) Spectra in H_2O buffer supplemented with 5 M NaCl at various delay times. (B) Kinetic traces (dots) and fits (solid curves) averaged over the probe bandwidth indicted by the blue vertical bar in panel (A) in H_2O buffer (blue), H_2O buffer supplemented with 5 M NaCl (olive), and D_2O buffer (red).

Proton inventory measurements. Having determined that the strong SKIE we observe corresponds to solvent-mediated ground state recovery from the $^3T_2$ state of ferrate(VI), we next performed a proton inventory study to gain a deeper understanding of this process by repeating the nanosecond-resolved OTA measurements in buffer solutions containing varying ratios of H_2O and D_2O. The kinetic traces (dots) and fits (solid curves) are plotted in Fig. 5A (the traces have been normalized to the maxima of their respective fits to facilitate comparison), which clearly illustrates the trend toward shorter $^3T_2$ lifetimes with increasing H_2O concentration. The time constants τ_4 obtained from the single-exponential fits are presented in Table 3, and the decay rates k_{obs} ($1/\tau_4$) are plotted vs. mole fraction χ in H_2O in the inset of Fig. 5A (95% confidence intervals indicated by error bars). Importantly, these data points follow a simple linear relationship ($R^2 = 0.979$), demonstrating that the relaxation process involves only a single

O-H bond.[37–39,55] We note, however, that this study does *not* provide a measure of q in Eqns. 1 and 2, the number of O-H bonds within the inner coordination sphere.

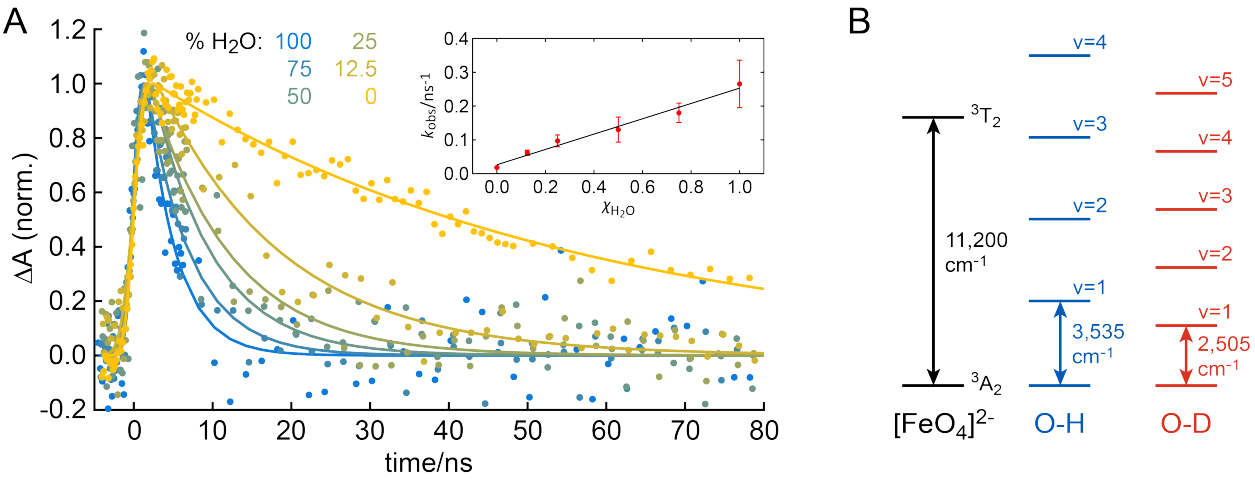

Figure 5. (A) Proton inventory study of nanosecond OTA kinetic traces of aqueous potassium ferrate(VI) following excitation at 560 nm. Data points (dots) correspond to the OTA signal averaged over the probe region centered at 650 nm shown in Fig. 3, normalized to the maximum of the corresponding single-exponential fit (solid curves). The percentage of H_2O comprising the solvent for each sample is indicated, with the remainder being D_2O; retardation of the ground state recovery with decreasing H_2O concentration is immediately apparent. (Inset) Plot of the nonradiative decay rate constant obtained from the exponential fits vs. mole fraction of H_2O in the solvent (red dots; 96% confidence intervals indicated by error bars) and corresponding linear fit (solid black line). (B) Relevant energy gaps for nonradiative relaxation of the lowest energy ^{3}MC state of aqueous ferrate(VI). The 11,200 cm^{-1} gap for the $^3T_2 \rightarrow {}^3A_2$ transition is shown alongside the overtones of the O-H and O-D vibrations that span that gap.

Table 3. Time constants for visible excitation on the nanosecond timescale

% H_2O	100	75	50	25	12.5	0
τ_4 (ns)	3.8 ± 1.0	5.6 ± 0.9	7.7 ± 2.2	10. ± 2	16 ± 2	55 ± 2

With this relaxation mechanism in mind, we may use the slope and intercept obtained from the linear regression shown in Fig. 5A to calculate the SKIE, starting from Eqn. 1. Because intermolecular deactivation does not appear to contribute significantly to the decay of the $^3T_2$ state, we may make the approximation that $k_{nr} = 0$ in Eqn. 1. And because aqueous ferrate(VI) is non-emissive at room temperature, $k_{rad} = 0$ as well. Thus, Eqn. 1 simplifies to:

$$k^{H_2O} = qk_{H_2O}, \qquad k^{D_2O} = qk_{D_2O} \tag{3}$$

We may then write the observed decay rate in a mixture of H_2O and D_2O as a linear combination of the rates in each pure solvent weighted by the mole fraction χ in H_2O:

$$k_{obs} = q\left[\chi k_{H_2O} + (1-\chi)k_{D_2O}\right] = q\left(k_{H_2O} - k_{D_2O}\right)\chi + qk_{D_2O} \tag{4}$$

From this equation, we can write expressions for the slope *m* and y-intercept *b* of the trendline in Fig. 5A as follows:

$$m = q\left(k_{H_2O} - k_{D_2O}\right) = 0.227\ \text{ns}^{-1} \tag{5}$$

and

$$b = qk_{D_2O} = 0.026\ \text{ns}^{-1} \tag{6}$$

Combining Eqns. 5 and 6, we can then calculate qk_{H_2O} and finally the SKIE:

$$qk_{H_2O} = m + qk_{D_2O} = 0.253\ \text{ns}^{-1} \tag{7}$$

$$\frac{qk_{H_2O}}{qk_{D_2O}} = 9.7 \tag{8}$$

Although we cannot determine the value of q, Eqn. 8 demonstrates that the SKIE may still be calculated without this information.

As discussed earlier, this large SKIE arises from the mismatch in the overtones of the acceptor modes (the O-H and O-D stretches) required to span the $^3T_2$ to $^3A_2$ energy gap in ferrate(VI), which we take to be approximately 11,200 cm^{-1} following the work of Al-Abdalla *et al*.[16] Using the fundamental stretching frequencies and anharmonicity constants of liquid water reported by Walrafen and Pugh,[71] we find that this gap falls between the third and fourth overtones of the O-H stretch but the fourth and fifth overtones of the O-D stretch. This is shown schematically in Fig. 5B.

It is notable that the SKIE of 9.7 reported here is commensurate with those measured for the *f-f* deactivation of lanthanide ions with similar energy gaps (Sm^{3+}, Dy^{3+}, Tb^{3+}, and Eu^{3+}).[49] Due to the Laporte-forbidden nature of the lanthanide transitions, the absolute rate constants of those deactivation processes are three to six orders of magnitude smaller than that of ferrate(VI). Nevertheless, the *ratios* of the rate constants in H_2O and D_2O simply reflect the energy gap of the transition. While some deviation from this trend would be observed in cases where radiative relaxation outpaces nonradiative relaxation in D_2O but not H_2O, such behavior is not expected for the non-emissive aqueous ferrate(VI) ion. Additionally, we note that 9.7 falls below the SKIE value of each of those four lanthanide ions but is still substantially higher than those typically observed for deactivation of organic chromophores. Thus, while the polyatomic nature of ferrate(VI) may facilitate energy transfer to the solvent and thereby result in a somewhat diminished SKIE in comparison to those of monatomic ions, this effect is quite moderate.

CONCLUSIONS

We have observed a dramatic impact on the relaxation dynamics of aqueous ferrate(VI) following either UV or visible excitation upon substitution of D_2O for H_2O and have identified

the nonradiative decay of the $^3T_2$ MC state to the ground $^3A_2$ state as the process that is most sensitive to this substitution. Using a combination of time-resolved optical and Fe K-edge spectroscopies, we have measured an SKIE of 9.7 for the $^3T_2 \rightarrow {}^3A_2$ transition, a value much closer to that observed for *f-f* transitions in aqueous lanthanide ions than for most polyatomic organic and inorganic chromophores. The linear dependence of decay rate constant on H_2O mole fraction observed via proton inventory studies confirms that a single O-H/O-D bond mediates the ground state recovery, which requires a higher overtone of the O-D stretch to span the energy gap compared to the O-H stretch. Solvent viscosity was found to play a negligible role in modulating the excited state dynamics.

As the only known shelf-stable Fe(VI) compounds, ferrate(VI) salts serve as excellent models of exotic hypervalent iron complexes. Because such species play crucial roles in the function of many bioinorganic systems, understanding how system-bath interactions impact the lifetimes, reactivities, and thermodynamic trajectories of model compounds like ferrate(VI) will guide efforts to elucidate and even control the catalytic cycles of metalloenzymes. Although changing the solvent environment is a blunt means of tuning these interactions, we have shown that simply lowering the frequency of a single vibrational mode to which ferrate(VI) is coupled dramatically extends the lifetime of one specific transient state while leaving all others largely unchanged. This result supports the possibility of controlling the behavior of iron-containing proteins through straightforward outer-sphere residue substitutions. Furthermore, extending the lifetimes of transient states of hypervalent iron species also has potential applications in water treatment and other areas of environmental science.

ASSOCIATED CONTENT

Supporting Information. Kinetic traces and corresponding fits with individual fit components shown, ground state Fe K-edge spectrum, and decay-associated spectra.

AUTHOR INFORMATION

Corresponding Author

*E-mail: dugan@uri.edu. ORCID: 0000-0003-4171-5179.

Present Addresses

†SLAC National Accelerator Laboratory, Menlo Park, California 94025, USA

Author Contributions

The manuscript was written through contributions of all authors. All authors have given approval to the final version of the manuscript.

ACKNOWLEDGMENT

This material is based on work supported by the U.S. Department of Energy, Office of Science, Office of Basic Energy Sciences under Award DE-SC0019429, which supported C.A., D.J.J., and D.H.; the U.S. National Science Foundation, Division of Chemical Bioengineering, Environmental, and Transport Systems (CBET) under CAREER Award 2046383, which supported J.E.G.; the U.S. Department of Energy, Office of Science, Office of Basic Energy Sciences, Chemical Sciences, Geosciences and Biosciences Division under Award DE-AC02-06CH11357, which supported G.D., A.M.M., and C.O.; and the U.S. Department of Energy, Office of Science, Office of Workforce Development for Teachers and Scientists, Office of Science Graduate Student Research (SCGSR) program, which also supported C.A. The SCGSR program is administered by the Oak Ridge Institute for Science and Education for the DOE

under contract number DE-SC0014664. This research used resources of the Advanced Photon Source, a U.S. Department of Energy (DOE) Office of Science User Facility operated for the DOE Office of Science by Argonne National Laboratory under Contract No. DE-AC02-06CH11357. All XTA data were collected at beamline 7-ID-D at the Advanced Photon Source, Argonne National Laboratory. The authors acknowledge and thank Ryan G. Hadt for helpful discussions and Element 26 Technology (400 Hobbs Road, Suite 107, League City, TX 77546; soundar.ramchandran@gmail.com; jtstrehl@gmail.com) for supplying the potassium ferrate(VI) used in this study.

ABBREVIATIONS

APS, advanced photon source; DAS, decay-associated spectrum/spectra; ESA, excited state absorption; FWHM, full width at half maximum; GSB, ground state bleach; IC, internal conversion; ISC, intersystem crossing; IRF, instrument response function; KIE, kinetic isotope effect; LMCT, ligand-to-metal charge transfer; MC, metal-centered; OTA, optical transient absorption; SKIE, solvent kinetic isotope effect; TA, transient absorption; UV, ultraviolet; XTA, X-ray transient absorption.

REFERENCES

(1) Denisov, I. G.; Makris, T. M.; Sligar, S. G.; Schlichting, I. Structure and Chemistry of Cytochrome P450. *Chem. Rev.* **2005**, *105* (6), 2253–2278. https://doi.org/10.1021/cr0307143.

(2) Shaik, S.; Kumar, D.; de Visser, S. P.; Altun, A.; Thiel, W. Theoretical Perspective on the Structure and Mechanism of Cytochrome P450 Enzymes. *Chem. Rev.* **2005**, *105* (6), 2279–2328. https://doi.org/10.1021/cr030722j.

(3) Huang, X.; Groves, J. T. Oxygen Activation and Radical Transformations in Heme Proteins and Metalloporphyrins. *Chem. Rev.* **2018**, *118* (5), 2491–2553. https://doi.org/10.1021/acs.chemrev.7b00373.

(4) Price, J. C.; Barr, E. W.; Tirupati, B.; Bollinger, J. Martin; Krebs, C. The First Direct Characterization of a High-Valent Iron Intermediate in the Reaction of an α-Ketoglutarate-Dependent Dioxygenase: A High-Spin Fe(IV) Complex in Taurine/α-Ketoglutarate Dioxygenase (TauD) from *Escherichia Coli*. *Biochemistry* **2003**, *42* (24), 7497–7508. https://doi.org/10.1021/bi030011f.

(5) Costas, M.; Mehn, M. P.; Jensen, M. P.; Que, L. Dioxygen Activation at Mononuclear Nonheme Iron Active Sites: Enzymes, Models, and Intermediates. *Chem. Rev.* **2004**, *104* (2), 939–986. https://doi.org/10.1021/cr020628n.

(6) Martinez, S.; Hausinger, R. P. Catalytic Mechanisms of Fe(II)- and 2-Oxoglutarate-Dependent Oxygenases. *Journal of Biological Chemistry* **2015**, *290* (34), 20702–20711. https://doi.org/10.1074/jbc.R115.648691.

(7) Galonić, D. P.; Barr, E. W.; Walsh, C. T.; Bollinger, J. M.; Krebs, C. Two Interconverting Fe(IV) Intermediates in Aliphatic Chlorination by the Halogenase CytC3. *Nat Chem Biol* **2007**, *3* (2), 113–116. https://doi.org/10.1038/nchembio856.

(8) Matthews, M. L.; Neumann, C. S.; Miles, L. A.; Grove, T. L.; Booker, S. J.; Krebs, C.; Walsh, C. T.; Bollinger, J. M. Substrate Positioning Controls the Partition between Halogenation and Hydroxylation in the Aliphatic Halogenase, SyrB2. *Proceedings of the National Academy of Sciences* **2009**, *106* (42), 17723–17728. https://doi.org/10.1073/pnas.0909649106.

(9) Li, J.; Liao, H.-J.; Tang, Y.; Huang, J.-L.; Cha, L.; Lin, T.-S.; Lee, J. L.; Kurnikov, I. V.; Kurnikova, M. G.; Chang, W.; *et al*. Epoxidation Catalyzed by the Nonheme Iron(II)- and 2-Oxoglutarate-Dependent Oxygenase, AsqJ: Mechanistic Elucidation of Oxygen Atom Transfer by a Ferryl Intermediate. *J. Am. Chem. Soc.* **2020**, *142* (13), 6268–6284. https://doi.org/10.1021/jacs.0c00484.

(10) Yu, C.-P.; Tang, Y.; Cha, L.; Milikisiyants, S.; Smirnova, T. I.; Smirnov, A. I.; Guo, Y.; Chang, W. Elucidating the Reaction Pathway of Decarboxylation-Assisted Olefination Catalyzed by a Mononuclear Non-Heme Iron Enzyme. *J. Am. Chem. Soc.* **2018**, *140* (45), 15190–15193. https://doi.org/10.1021/jacs.8b10077.

(11) Carrington, A.; Schonland, D.; Symons, M. C. R. Structure and Reactivity of the Oxyanions of Transition Metals. Part IV. Some Relations between Electronic Spectra and Structure. *J. Chem. Soc.* **1957**, No. 0, 659–665. https://doi.org/10.1039/JR9570000659.

(12) Orgel, L. E. The Visible Spectrum of the Hypomanganate Ion. *Mol. Phys.* **1964**, *7* (4), 397–399. https://doi.org/10.1080/00268976300101161.

(13) Itoh, Y. Single-Crystal Electronic Absorption Spectra of $MMnO_4$ (M=K, Rb, Cs), K_2CrO_4, K_2MnO_4, and K_2FeO_4. *J. Spectrosc. Soc. Japan* **1976**, *25* (2), 83–93. https://doi.org/10.5111/bunkou.25.83.

(14) Herren, M.; Güdel, H. U. Ferrate(VI), a Novel near-Infrared Luminophore. *Inorg. Chem.* **1992**, *31* (18), 3683–3684. https://doi.org/10.1021/ic00044a001.

(15) Brunold, T. C.; Güdel, H. U.; Kück, S.; Huber, G. Excited State Properties of Ferrate(VI) Doped Crystals of K_2SO_4 and K_2CrO_4. *J. Lumin.* **1996**, *65*, 293–301. https://doi.org/10.1016/0022-2313(95)00082-8.

(16) Al-Abdalla, A.; Seijo, L.; Barandiarán, Z. A New Interpretation of the Bonding and Spectroscopy of the Tetraoxoferrate(VI) FeO_4^{2-} Ion. *J. Chem. Phys.* **1998**, *109* (15), 6396–6405. https://doi.org/10.1063/1.477283.

(17) Antolini, C.; Jr, C. D. S.; Otolski, C. J.; Doumy, G.; March, A. M.; Walko, D. A.; Liu, C.; Zhang, X.; Young, B. T.; Goodwill, J. E.; Hayes, D. Photochemical and Photophysical Dynamics of the Aqueous Ferrate(VI) Ion. *J. Am. Chem. Soc.* **2022**, *144* (49), 22514–22527. https://doi.org/10.1021/jacs.2c08048.

(18) Stryer, L. Excited-State Proton-Transfer Reactions. A Deuterium Isotope Effect on Fluorescence. *J. Am. Chem. Soc.* **1966**, *88* (24), 5708–5712. https://doi.org/10.1021/ja00976a004.

(19) Moog, R. S.; Maroncelli, M. 7-Azaindole in Alcohols: Solvation Dynamics and Proton Transfer. *J. Phys. Chem.* **1991**, *95* (25), 10359–10369. https://doi.org/10.1021/j100178a023.

(20) Chen, Y.; Gai, F.; Petrich, J. W. Solvation of 7-Azaindole in Alcohols and Water: Evidence for Concerted, Excited-State, Double-Proton Transfer in Alcohols. *J. Am. Chem. Soc.* **1993**, *115* (22), 10158–10166. https://doi.org/10.1021/ja00075a035.

(21) Kaizer, J.; Klinker, E. J.; Oh, N. Y.; Rohde, J.-U.; Song, W. J.; Stubna, A.; Kim, J.; Münck, E.; Nam, W.; Que, L. Nonheme $Fe^{IV}O$ Complexes That Can Oxidize the C–H Bonds of

Cyclohexane at Room Temperature. *J. Am. Chem. Soc.* **2004**, *126* (2), 472–473. https://doi.org/10.1021/ja037288n.

(22) Klinker, E. J.; Shaik, S.; Hirao, H.; Que Jr., L. A Two-State Reactivity Model Explains Unusual Kinetic Isotope Effect Patterns in C–H Bond Cleavage by Nonheme Oxoiron(IV) Complexes. *Angewandte Chemie International Edition* **2009**, *48* (7), 1291–1295. https://doi.org/10.1002/anie.200804029.

(23) Adhikary, R.; Mukherjee, P.; Kee, T. W.; Petrich, J. W. Excited-State Intramolecular Hydrogen Atom Transfer and Solvation Dynamics of the Medicinal Pigment Curcumin. *J. Phys. Chem. B* **2009**, *113* (15), 5255–5261. https://doi.org/10.1021/jp901234z.

(24) Bunton, C. A.; Shiner, V. J. Isotope Effects in Deuterium Oxide Solution. Part II. Reaction Rates in Acid, Alkaline and Neutral Solution, Involving Only Secondary Solvent Effects. *J. Am. Chem. Soc.* **1961**, *83* (15), 3207–3214. https://doi.org/10.1021/ja01476a010.

(25) Hardy, L. W.; Kirsch, J. F. pH Dependence and Solvent Deuterium Oxide Kinetic Isotope Effects on *Bacillus Cereus* β-Lactamase I Catalyzed Reactions. *Biochemistry* **1984**, *23* (6), 1282–1287. https://doi.org/10.1021/bi00301a041.

(26) Rodriguez, E. J.; Angeles, T. S.; Meek, T. D. Use of Nitrogen-15 Kinetic Isotope Effects to Elucidate Details of the Chemical Mechanism of Human Immunodeficiency Virus 1 Protease. *Biochemistry* **1993**, *32* (46), 12380–12385. https://doi.org/10.1021/bi00097a015.

(27) Hille, R. Electron Transfer within Xanthine Oxidase: A Solvent Kinetic Isotope Effect Study. *Biochemistry* **1991**, *30* (35), 8522–8529. https://doi.org/10.1021/bi00099a004.

(28) Westphal, K. L.; Tommos, C.; Cukier, R. I.; Babcock, G. T. Concerted Hydrogen-Atom Abstraction in Photosynthetic Water Oxidation. *Current Opinion in Plant Biology* **2000**, *3* (3), 236–242. https://doi.org/10.1016/S1369-5266(00)80071-0.

(29) Ghosh, I.; Khan, S.; Banerjee, G.; Dziarski, A.; Vinyard, D. J.; Debus, R. J.; Brudvig, G. W. Insights into Proton-Transfer Pathways during Water Oxidation in Photosystem II. *J. Phys. Chem. B* **2019**, *123* (39), 8195–8202. https://doi.org/10.1021/acs.jpcb.9b06244.

(30) Chen, Z.; Concepcion, J. J.; Hu, X.; Yang, W.; Hoertz, P. G.; Meyer, T. J. Concerted O Atom–Proton Transfer in the O–O Bond Forming Step in Water Oxidation. *Proceedings of the National Academy of Sciences* **2010**, *107* (16), 7225–7229. https://doi.org/10.1073/pnas.1001132107.

(31) Coggins, M. K.; Zhang, M.-T.; Vannucci, A. K.; Dares, C. J.; Meyer, T. J. Electrocatalytic Water Oxidation by a Monomeric Amidate-Ligated Fe(III)–Aqua Complex. *J. Am. Chem. Soc.* **2014**, *136* (15), 5531–5534. https://doi.org/10.1021/ja412822u.

(32) Du, H.-Y.; Chen, S.-C.; Su, X.-J.; Jiao, L.; Zhang, M.-T. Redox-Active Ligand Assisted Multielectron Catalysis: A Case of Co^{III} Complex as Water Oxidation Catalyst. *J. Am. Chem. Soc.* **2018**, *140* (4), 1557–1565. https://doi.org/10.1021/jacs.8b00032.

(33) Schulze, M.; Kunz, V.; Frischmann, P. D.; Würthner, F. A Supramolecular Ruthenium Macrocycle with High Catalytic Activity for Water Oxidation That Mechanistically Mimics Photosystem II. *Nature Chem* **2016**, *8* (6), 576–583. https://doi.org/10.1038/nchem.2503.

(34) Krishtalik, L. I. On the Theory of the 'Proton Inventory' Method. *Mendeleev Communications* **1993**, *3* (2), 66–67. https://doi.org/10.1070/MC1993v003n02ABEH000227.

(35) Gai, F.; Rich, R. L.; Chen, Y.; Petrich, J. W. Probing Solvation by Alcohols and Water with 7-Azaindole. In *Structure and Reactivity in Aqueous Solution*; ACS Symposium Series; American Chemical Society, 1994; Vol. 568, pp 182–195. https://doi.org/10.1021/bk-1994-0568.ch013.

(36) Jenson, D. L.; Barry, B. A. Proton-Coupled Electron Transfer in Photosystem II: Proton Inventory of a Redox Active Tyrosine. *J. Am. Chem. Soc.* **2009**, *131* (30), 10567–10573. https://doi.org/10.1021/ja902896e.

(37) Ermolaev, V. L.; Sveshnikova, E. B.; Bodunov, E. N. Inductive-Resonant Mechanism of Nonradiative Transitions in Ions and Molecules in Condensed Phase. *Phys.-Usp.* **1996**, *39* (3), 261. https://doi.org/10.1070/PU1996v039n03ABEH000137.

(38) Fitzpatrick, P. F. Combining Solvent Isotope Effects with Substrate Isotope Effects in Mechanistic Studies of Alcohol and Amine Oxidation by Enzymes. *Biochim Biophys Acta* **2015**, *1854* (11), 1746–1755. https://doi.org/10.1016/j.bbapap.2014.10.020.

(39) Shamsipur, M.; Ardeshiri, M.; Avat (Arman) Taherpour; Pashabadi, A. Unveiling the Mechanistic Implications of Water Oxidation Reactions Boosted by Guanidine Proton Relays: A Chemical-Electrochemical-Chemical Pathway and a Non-Concerted Proton-Electron Transfer. *Journal of Materials Chemistry A* **2021**, *9* (5), 2937–2947. https://doi.org/10.1039/D0TA10641K.

(40) Robinson, G. W. Spectra and Energy Transfer Phenomena in Crystalline Rare Gas Solvents. *Journal of Molecular Spectroscopy* **1961**, *6*, 58–83. https://doi.org/10.1016/0022-2852(61)90233-8.

(41) Robinson, G. W.; Frosch, R. P. Theory of Electronic Energy Relaxation in the Solid Phase. *The Journal of Chemical Physics* **1963**, *37* (9), 1962–1973. https://doi.org/10.1063/1.1733413.

(42) Robinson, G. W.; Frosch, R. P. Electronic Excitation Transfer and Relaxation. *The Journal of Chemical Physics* **1962**, *38* (5), 1187–1203. https://doi.org/10.1063/1.1733823.

(43) Alarcon, E. I.; González-Béjar, M.; Montes-Navajas, P.; Garcia, H.; Lissi, E. A.; Scaiano, J. C. Unexpected Solvent Isotope Effect on the Triplet Lifetime of Methylene Blue Associated to Cucurbit[7]Uril. *Photochem. Photobiol. Sci.* **2012**, *11* (2), 269–273. https://doi.org/10.1039/C1PP05227F.

(44) Beeby, A.; Parker, A. W.; Simpson, M. S. C.; Phillips, D. The Effect of Solvent Deuteration on the Photophysics of Sulphonated Aluminium Phthalocyanine. *Journal of Photochemistry and Photobiology B: Biology* **1992**, *16* (1), 73–81. https://doi.org/10.1016/1011-1344(92)85154-M.

(45) Yuan, D.; Brown, R. G. Enhanced Nonradiative Decay in Aqueous Solutions of Aminonaphthalimide Derivatives via Water-Cluster Formation. *J. Phys. Chem. A* **1997**, *101* (19), 3461–3466. https://doi.org/10.1021/jp964061o.

(46) Haas, Y.; Stein, G. Pathways of Radiative and Radiationless Transitions in Europium(III) Solutions. Role of Solvents and Anions. *J. Phys. Chem.* **1971**, *75* (24), 3668–3677. https://doi.org/10.1021/j100693a005.

(47) Haas, Y.; Stein, G. Pathways of Radiative and Radiationless Transitions in Europium(III) Solutions. The Role of High Energy Vibrations. *J. Phys. Chem.* **1971**, *75* (24), 3677–3681. https://doi.org/10.1021/j100693a006.

(48) Haas, Y.; Stein, G. Radiative and Nonradiative Pathways in Solutions. Excited States of the Europium(III) Ion. *J. Phys. Chem.* **1972**, *76* (8), 1093–1104. https://doi.org/10.1021/j100652a002.

(49) Stein, G.; Würzberg, E. Energy Gap Law in the Solvent Isotope Effect on Radiationless Transitions of Rare Earth Ions. *J. Chem. Phys.* **1975**, *62* (1), 208. https://doi.org/10.1063/1.430264.

(50) Tanaka, F.; Yamashita, S. Luminescence Lifetimes of Aqueous Europium Chloride, Nitrate, Sulfate, and Perchlorate Solutions. Studies on the Nature of the Inner Coordination Sphere of Europium(III) Ion. *Inorg. Chem.* **1984**, *23* (14), 2044–2046. https://doi.org/10.1021/ic00182a013.

(51) Bünzli, J.-C. G.; Eliseeva, S. V. Basics of Lanthanide Photophysics. In *Lanthanide Luminescence*; Hänninen, P., Härmä, H., Eds.; Springer Series on Fluorescence; Springer Berlin Heidelberg: Berlin, Heidelberg, 2010; Vol. 7, pp 1–45. https://doi.org/10.1007/4243_2010_3.

(52) Mortensen, S. S.; Marciniak Nielsen, M. A.; Nawrocki, P.; Sørensen, T. J. Electronic Energy Levels and Optical Transitions in Samarium(III) Solvates. *J. Phys. Chem. A* **2022**, *126* (46), 8596–8605. https://doi.org/10.1021/acs.jpca.2c04793.

(53) Horrocks, W. DeW.; Sudnick, D. R. Lanthanide Ion Probes of Structure in Biology. Laser-Induced Luminescence Decay Constants Provide a Direct Measure of the Number of

Metal-Coordinated Water Molecules. *J. Am. Chem. Soc.* **1979**, *101* (2), 334–340. https://doi.org/10.1021/ja00496a010.

(54) Quici, S.; Cavazzini, M.; Raffo, M. C.; Botta, M.; Giovenzana, G. B.; Ventura, B.; Accorsi, G.; Barigelletti, F. Luminescence Properties and Solution Dynamics of Lanthanide Complexes Composed by a Macrocycle Hosting Site and Naphthalene or Quinoline Appended Chromophore. *Inorganica Chimica Acta* **2007**, *360* (8), 2549–2557. https://doi.org/10.1016/j.ica.2006.12.040.

(55) Heller, A. Formation of Hot OH Bonds in the Radiationless Relaxations of Excited Rare Earth Ions in Aqueous Solutions. *J. Am. Chem. Soc.* **1966**, *88* (9), 2058–2059. https://doi.org/10.1021/ja00961a046.

(56) Horrocks, W. D.; Sudnick, D. R. Lanthanide Ion Luminescence Probes of the Structure of Biological Macromolecules. *Acc. Chem. Res.* **1981**, *14* (12), 384–392. https://doi.org/10.1021/ar00072a004.

(57) March, A. M.; Stickrath, A.; Doumy, G.; Kanter, E. P.; Krässig, B.; Southworth, S. H.; Attenkofer, K.; Kurtz, C. A.; Chen, L. X.; Young, L. Development of High-Repetition-Rate Laser Pump/X-Ray Probe Methodologies for Synchrotron Facilities. *Review of Scientific Instruments* **2011**, *82* (7), 073110. https://doi.org/10.1063/1.3615245.

(58) Walko, D. A.; Adams, B. W.; Doumy, G.; Dufresne, E. M.; Li, Y.; March, A. M.; Sandy, A. R.; Wang, J.; Wen, H.; Zhu, Y. Developments in Time-Resolved X-Ray Research at APS Beamline 7ID. *AIP Conference Proceedings* **2016**, *1741* (1), 030048. https://doi.org/10.1063/1.4952871.

(59) March, A. M.; Doumy, G.; Andersen, A.; Al Haddad, A.; Kumagai, Y.; Tu, M.-F.; Bang, J.; Bostedt, C.; Uhlig, J.; Nascimento, D. R.; *et al*. Elucidation of the Photoaquation Reaction Mechanism in Ferrous Hexacyanide Using Synchrotron X-Rays with Sub-Pulse-Duration Sensitivity. *J. Chem. Phys.* **2019**, *151* (14), 144306. https://doi.org/10.1063/1.5117318.

(60) Sharma, V. K. Ferrate(V) Oxidation of Pollutants: A Premix Pulse Radiolysis Study. *Radiat. Phys. Chem.* **2002**, *65* (4), 349–355. https://doi.org/10.1016/S0969-806X(02)00335-3.

(61) Rush, J. D.; Bielski, B. H. J. Decay of Ferrate(V) in Neutral and Acidic Solutions. A Premix Pulse Radiolysis Study. *Inorg. Chem.* **1994**, *33* (24), 5499–5502. https://doi.org/10.1021/ic00102a024.

(62) Bielski, B. H. J.; Thomas, M. J. Studies of Hypervalent Iron in Aqueous Solutions. 1. Radiation-Induced Reduction of Iron(VI) to Iron(V) by CO_2^-. *J. Am. Chem. Soc.* **1987**, *109* (25), 7761–7764. https://doi.org/10.1021/ja00259a026.

(63) Rush, J. D.; Bielski, B. H. J. Kinetics of Ferrate(V) Decay in Aqueous Solution. A Pulse-Radiolysis Study. *Inorg. Chem.* **1989**, *28* (21), 3947–3951. https://doi.org/10.1021/ic00320a004.

(64) Bielski, B. H. J.; Sharma, V. K.; Czapski, G. Reactivity of Ferrate(V) with Carboxylic Acids: A Pre-Mix Pulse Radiolysis Study. *Radiat. Phys. Chem.* **1994**, *44* (5), 479–484. https://doi.org/10.1016/0969-806X(94)90044-2.

(65) Sharma, V. K.; Rivera, W.; Joshi, V. N.; Millero, F. J.; O'Connor, D. Ferrate(VI) Oxidation of Thiourea. *Environ. Sci. Technol.* **1999**, *33* (15), 2645–2650. https://doi.org/10.1021/es981083a.

(66) Chou, J.; Zhao, Y.; Li, X.-T.; Wang, W.-P.; Tan, S.-J.; Wang, Y.-H.; Zhang, J.; Yin, Y.-X.; Wang, F.; Xin, S.; *et al*. Hydrogen Isotope Effects on Aqueous Electrolyte for Electrochemical Lithium-Ion Storage. *Angewandte Chemie* **2022**, *134* (25), e202203137. https://doi.org/10.1002/ange.202203137.

(67) Sharafy, S.; Muszkat, K. A. Viscosity Dependence of Fluorescence Quantum Yields. *J. Am. Chem. Soc.* **1971**, *93* (17), 4119–4125. https://doi.org/10.1021/ja00746a004.

(68) Cremers, D. A.; Windsor, M. W. A Study of the Viscosity-Dependent Electronic Relaxation of Some Triphenylmethane Dyes Using Picosecond Flash Photolysis. *Chemical Physics Letters* **1980**, *71* (1), 27–32. https://doi.org/10.1016/0009-2614(80)85283-3.

(69) Bergamasco, S.; Calzaferri, G.; Hädener, K. Solute-Solvent Relaxation of Electronically Excited Xanthene Dyes. *Journal of Photochemistry and Photobiology A: Chemistry* **1990**, *53* (1), 109–125. https://doi.org/10.1016/1010-6030(90)87117-T.

(70) Kestin, J.; Khalifa, H. E.; Correia, R. J. Tables of the Dynamic and Kinematic Viscosity of Aqueous NaCl Solutions in the Temperature Range 20–150 °C and the Pressure Range 0.1–35 MPa. *Journal of Physical and Chemical Reference Data* **1981**, *10* (1), 71–88. https://doi.org/10.1063/1.555641.

(71) Walrafen, G. E.; Pugh, E. Raman Combinations and Stretching Overtones from Water, Heavy Water, and NaCl in Water at Shifts to ca. 7000 Cm^{-1}. *Journal of Solution Chemistry* **2004**, *33* (1), 81–97. https://doi.org/10.1023/B:JOSL.0000026646.33891.a8.

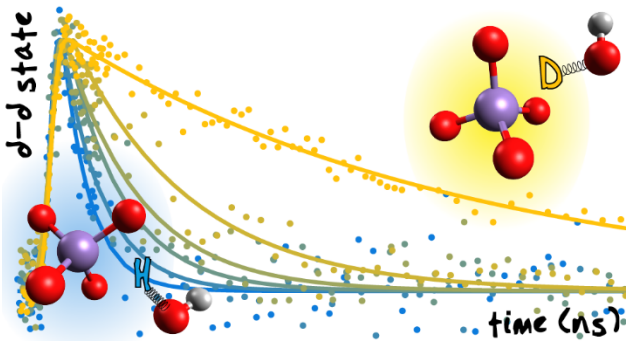

TOC Graphic